

A model of \bar{n} annihilation in experimental searches for $n \rightarrow \bar{n}$ transformations

Authors

E. S. Golubeva¹, J. L. Barrow², C. G. Ladd²

¹*Institute for Nuclear Research, Russian Academy of Sciences, Prospekt 60-letiya Oktyabrya 7a, Moscow, 117312, Russia*

²*University of Tennessee, Department of Physics, 401 Nielsen Physics Building, 1408 Circle Drive, Knoxville, TN 37996, USA*

Abstract

Searches for baryon number violation are expected to play an important role in the evolution of our understanding of beyond standard model physics, including searches for proton decay and neutron-antineutron transformation ($n \rightarrow \bar{n}$). The latter is a key prediction of certain popular theories of baryogenesis, and the experiments such as the Deep Underground Neutrino Experiment and the European Spallation Source plan to search for this process with bound- and free-neutron systems. Accurate simulation of this process in Monte Carlo will be important for proper reconstruction of these rare events. This article presents recent developments towards accurate simulation of the annihilation process for use in a cold, free neutron beam for $n \rightarrow \bar{n}$ searches from $\bar{n}C$ annihilation, as $^{12}_6C$ is the target of choice for the European Spallation Source's NNbar Collaboration. Initial efforts are made in this paper to perform analogous studies for intranuclear transformation searches in $^{40}_{18}Ar$ nuclei, although this latter work is in its preliminary stages. Such future work looks forward to the Deep Underground Neutrino Experiment's searches for intranuclear $n \rightarrow \bar{n}$ searches.

1. Introduction

Experimental searches for baryon number violating processes, in particular, neutron—antineutron oscillation ($n \rightarrow \bar{n}$), are of great importance due to their possible connections to the explanations of the observed matter-antimatter asymmetry of the universe, as first laid down by V. A. Kuzmin (INR RAS, Moscow) [1]. As early as 1967, A. Sakharov pointed out [2] that for the explanation of the Baryon Asymmetry of the Universe, besides departure from thermal equilibrium and CP symmetry, there should exist interactions in which baryonic charge is violated. In the Standard Model of particle physics, the violation of CP symmetry is not strong enough to explain the observed baryon asymmetry of the universe.

In Grand Unification Theories and some SM extensions, it is possible to violate baryon number by a single unit ($\Delta B = \pm 1$), which makes proton decay possible: $p \rightarrow e^+\pi^0$. However, some models may have processes in which baryon number can be violated by two units: $\Delta B = \pm 2$. Thus, it becomes possible for a neutron to transform into an antineutron, and back, i.e. *neutron—antineutron oscillations*. There has been no experimental confirmation of any process which violated baryon number. Thus, the search for $n \rightarrow \bar{n}$, along with proton decay, is one of the most important areas of modern physics, hopefully leading to an understanding of phenomena beyond the Standard Model.

There are two possible ways to search for $n \rightarrow \bar{n}$ in free space: high-intensity neutron beams from nuclear reactors, or neutron beams generated via spallation from high energy accelerators. The best result in the measurement of the oscillation period, $\tau_{n \rightarrow \bar{n}}$, was attained at the Institut Laue-Langevin (ILL) in Grenoble, France, from a reactor of cold neutrons with an average velocity of $700 \frac{m}{s}$; these

neutrons flew through an evacuated, magnetically shielded pipe of 76 m in length (corresponding to a flight time of ~ 0.1 s), until being allowed to hit a target of carbon foil (with a thickness of ~ 130 μm). For normal neutrons, the target was effectively transparent, while it instead absorbed antineutrons, resulting in matter-antimatter annihilation. Detectors surrounded the target to record such annihilation events. In total, the target received $\sim 3 \times 10^{18}$ neutrons, with no recorded annihilation events. As a result, the oscillation period for free neutrons was established [3] to be

$$\tau_{n \rightarrow \bar{n}} \geq 0.86 \times 10^8 \text{ s.} \quad (1)$$

More accurately, considering (1), this should not be called an oscillation time, but instead a neutron—antineutron *transformation* time, because it is much longer than the neutron's lifetime. In the last two decades since obtaining this result, there has been significant technological developments in planning another transformation experiment. A new experiment has recently been proposed to find the transformation at the European Spallation Source (ESS) neutron beam [4], currently under construction. According to preliminary estimates, such an experiment could improve the results obtain by ILL by 2 – 3 orders of magnitude.

Another way to find the $n \rightarrow \bar{n}$ transformation is with intranuclear searches. Indirect restrictions on $\tau_{n \rightarrow \bar{n}}$ can be obtained from experiments with large underground detectors looking for any hint of the instability of matter. Transformation of a neutron into an antineutron within the nucleus would lead to its annihilation with another neighboring nucleon, resulting in the release of ~ 2 GeV of total energy. However, such transformations are significantly suppressed compared to free neutron transformations in vacuum [4]. The limit on the $n \rightarrow \bar{n}$ intranuclear transformation time (in *matter*, m) τ_m is associated with the square of the free transformation time through a dimensional suppression factor, R :

$$\tau_m = R \cdot \tau_{n \rightarrow \bar{n}}^2 \quad (2)$$

In the nucleus, this suppression is due to differences between the neutron and antineutron nuclear potentials; however, in high mass detectors, this suppression can be compensated by the huge number of neutrons available for investigation within the large detector volume. A number of major collaborations have been involved in the search for such events in nuclei, such as Super-Kamiokande in $^{16}_8O$, and Soudan-2 in $^{56}_{26}Fe$. In the Soudan-2 experiment, there is a limit on the transformation time in iron nuclei of $\tau_{Fe} \geq 7.2 \times 10^{31}$ $yr s$ [5], which is in line with a limit for the free transformation time of $\tau_{n \rightarrow \bar{n}} = 1.3 \times 10^8 s$.

Future experiments in large underground detectors can improve the restrictions on processes where $\Delta B = \pm 2$ up to $\sim 10^{33} - 10^{35}$ $yr s$ [4]. An experiment is currently proposed to search for $n \rightarrow \bar{n}$ in the $^{40}_{18}Ar$ nucleus using the large liquid argon detector currently under construction: the Deep Underground Neutrino Experiment (DUNE) [6].

Next generation free neutron experiments can reach the lower limits of the $\tau_{n \rightarrow \bar{n}} \sim 10^9 - 10^{10}$ s range. Whether or not $n \rightarrow \bar{n}$ is found, the transformation time in these experiments depends critically on the energy scale at which the new BSM physics begins is not known. In any case, such results will be of great importance in understanding fundamental properties of matter, along with building a precise theoretical model describing these properties.

From the estimate of the magnitude of the transformation period $\tau_{n \rightarrow \bar{n}} \geq 10^8 s$, it follows that the expected effect is very small. For a thermal neutron beam, the admixture of antineutrons is less than

$\frac{\bar{n}}{n} < 10^{-18}$ [7]. Therefore, the experiment requires maximum efficiency for detection and reconstruction of incredibly rare antineutrons. Thus, one requires detailed information about the processes during the annihilation of slow antineutrons on nuclei. The purpose of this work is to create a model to describe the annihilation of the slow antineutrons incident upon carbon nuclei for the upcoming transformation experiment using a free neutron beam at ESS [4]. The first steps have also been taken towards a full simulation of the annihilation resulting from $n \rightarrow \bar{n}$ within ${}^{40}_{18}\text{Ar}$ nuclei, to be used in DUNE [6].

In the framework of this proposed model, the annihilation of an antineutron on the nucleus is considered to consist of several sequential and independent stages. In this approach, as the initial step, one defines the absorption point of an antineutron by the nucleus. This initial stage for annihilation of the slow antineutron on the carbon nucleus is considered within the optical model. For argon, the $n \rightarrow \bar{n}$ transformation is assumed to occur within the nucleus, and will be the focus of future work. All subsequent stages of the process for both carbon and argon do not differ, and are considered within a unified approach. The second stage of the process is the actual annihilation of the antineutron with one of the constituent intranuclear nucleons. The third stage is the intranuclear cascade (INC), initiated by the emergence of mesons from the annihilation. In the final stage, we have de-excitation of the residual nucleus. Section 2 provides a detailed description of the model for all successive stages of the process under consideration. In Section 3, a comparison will be made between simulation and experiment to test the model against at-rest $\bar{p}C$ annihilation data. In Section 4, some validation tests of the $\bar{n}C$ annihilation event generator output data are shown. In Section 5, we summarize our work, and briefly consider a future path toward simulation of intranuclear transformations in argon.

2. The model of the antineutron annihilation on the nucleus

2.1 Absorption of the slow antineutron by the ${}^{12}_6\text{C}$ nucleus

The approach used to describe the interaction between the nucleus and the incoming slow antineutron resulting from the transformation is based on the integration of optical and cascade models. In the optical-cascade model, the initial conditions for the intranuclear cascade (INC) are formulated within the optical model. This approach was first successfully applied in [8] to describe the annihilation of stopping antiprotons on nuclei when the antiproton is absorbed from the bound state made by the antiproton orbiting the atom. The solution for the antineutron was performed by L. A. Kondratyuk [9,10] when preparing for discussions of a planned $n \rightarrow \bar{n}$ search experiment using high-intensity neutrons (at ~ 40 K) at the High-Flux Isotope Reactor (HFIR) at Oak Ridge National Laboratory (ORNL) [11]. Unlike an antiproton in a Coulomb bound state, the slow antineutron is absorbed by the nucleus from an S -wave state; the antineutron wave function comes from the solution of the wave equation:

$$(\vec{\nabla}^2 + k^2)\Psi(\vec{r}) = V_{opt}(\vec{r})\Psi(\vec{r}), \quad (3)$$

where k is the antineutron momentum. The complex optical potential is defined by the expression:

$$V_{opt}(\vec{r}) = -4\pi[f_{\bar{n}p}(0)\rho_p(\vec{r}) + f_{\bar{n}n}(0)\rho_n(\vec{r})], \quad (4)$$

where $f_{\bar{n}p}(0)$ and $f_{\bar{n}n}(0)$ are the $\bar{n}p$ and $\bar{n}n$ forward scattering amplitudes in the laboratory coordinate system, while $\rho_p(\vec{r})$ and $\rho_n(\vec{r})$ are the proton and neutron densities, respectively. For ${}^{12}_6\text{C}$, we take $\rho_p(\vec{r}) = \rho_n(\vec{r}) = \rho(\vec{r})$.

For the numerical solution to this equation, the potential was divided into N radial zones, each with constant density. In each, for the j th-zone, the radial wave function has been assumed to take the form:

$$\tilde{\phi}_j(r) = r\Psi_j(r) = A_j e^{ik_j r} - B_j e^{-ik_j r}, \quad (5)$$

where $k_j^2 = k^2 - V_{opt}(r_j)$, and where complex constants A_j and B_j are due to continuity condition for $\tilde{\phi}(r)$ and $\tilde{\phi}'(r)$. Initial boundary conditions have been adopted such that $A = B = 1$ when $r = 0$, and then, when $r \gg R$, the solution takes the form:

$$\tilde{\phi}(r) = A_\infty \frac{\sin(kr + \delta)}{k}, \quad (6)$$

where $\delta = -ka_{\bar{n}A}$, with $a_{\bar{n}A}$ being the complex scattering length. For small k , the asymptotic solution seen in (6) becomes:

$$\tilde{\phi}(r) = A_\infty (r - a_{\bar{n}A}). \quad (7)$$

After we have found A_∞ and δ , the solution can be renormalized by dividing by A_∞ :

$$\phi(r) = \frac{1}{A_\infty} \tilde{\phi}(r). \quad (8)$$

The imaginary part of the $\bar{n}A$ scattering amplitude can also be found from the expression:

$$Im[f_{\bar{n}A}(0)] = -Im[a_{\bar{n}A}] = 4\pi \int Im[V_{opt}(r) |\phi(r)|^2] dr. \quad (9)$$

Therefore, the correct solution can be verified by comparing $Im[a_{\bar{n}A}]$ from expressions (7) and (9).

Real and imaginary parts to the $\bar{p}p$ scattering lengths are known from the widths and shifts in $\bar{p}p$ atomic levels. Various experiments have given us values of $Re[a_{\bar{p}p}]$ and $Im[a_{\bar{p}p}]$ within the following limits [12]: $Re[a_{\bar{p}p}] = 0.7 - 1.2 \text{ fm}$ and $Im[a_{\bar{p}p}] = -(0.6 - 1.3) \text{ fm}$. The imaginary part of the $\bar{n}p$ scattering length was taken from the OBELIX collaboration data [13]: $Im[a_{\bar{n}p}] \approx 0.3 - 0.5 \text{ fm}$. The value of the real part of the $\bar{n}p$ scattering length could not be determined due to the large experimental uncertainty. Therefore, the real and imaginary parts for the $\bar{n}A$ scattering lengths were calculated for different amplitude values of elementary $\bar{n}N$ scattering, as was defined in [10]. These take the form of (assuming that $a_{\bar{n}n} = a_{\bar{p}p}$):

$$f_{\bar{n}N}(0) = -2 \left(\frac{Z}{A} a_{\bar{n}p} + \frac{N}{A} a_{\bar{n}n} \right). \quad (10)$$

The wave equation was solved numerically for different amplitude values of $f_{\bar{n}N}(0)$ [10]; as a result, a value was selected of $f_{\bar{n}N}(0) = -1.0 + 1.7i \text{ fm}$.

The radial distribution of the nuclear density is directly related to the antineutron absorption probability; thus, for a carbon nucleus, one has:

$$P_{abs}(r) \sim \rho(r) |\phi(r)|^2. \quad (11)$$

This radial dependence of $P_{abs}(r)$ for the $^{12}_6\text{C}$ nucleus, derived from the wave equation, is shown in Figure 3 of paper [10]. However, for the future use of $P_{abs}(r)$, in order to define the annihilation point precisely within the optical-cascade model, it is desirable to have a simple analytic function instead.

Therefore, we approximate $P_{abs}(r)$ as a Gaussian, with a maximum situated at $r = c + 1.2 fm$ —where c is the radius of half density (where $c(^{12}_6C) = 2.0403 fm$)—and a variance of $\sigma = 1 fm$. Thus, for our simulation, we use a radial distribution of absorption probability for a slow antineutron by a carbon nucleus, $P_{abs}(r)$ (see Figure 1). For comparison, the same figure shows $P_{abs}(r)$ for stopping antiprotons, seen in [8].

The model assumes that the proton density within the nucleus $\rho(r)$ is described as an electrical charge distribution, which is obtained from high-energy electron scattering experiments. The function $\rho(r)$ obeys the distribution of Fermi:

$$\frac{\rho(r)}{\rho(0)} = \left[1 + e^{\frac{r-c}{a}} \right]^{-1}, \quad (12)$$

where $a = 0.5227 fm$ is the diffuseness parameter of the nucleus, and c the radius of half density [14]. For practical reasons, in the modeling process, the nucleus is split into seven concentric zones, within which the nucleon density is considered to be constant. This way, we can approximate the original density distribution, $\rho(r)$, quite well. Figure 1 shows the density distribution of the nucleons for $^{12}_6C$, calculated by equation (12), along with the approximation which divides the nucleus into seven zones of constant density. Since an antineutron would be strongly absorbed even within the diffuse periphery of a nuclear substance, another eighth zone with density $\rho_{out} = 0.001 \cdot \rho(7)$ is added which extends far beyond the nuclear envelope. Neutrons are considered to be distributed throughout the nucleus in the same way as protons in equation (12); therefore, for $^{12}_6C$, the distribution of proton and neutron density $\rho(r)$ is identical.

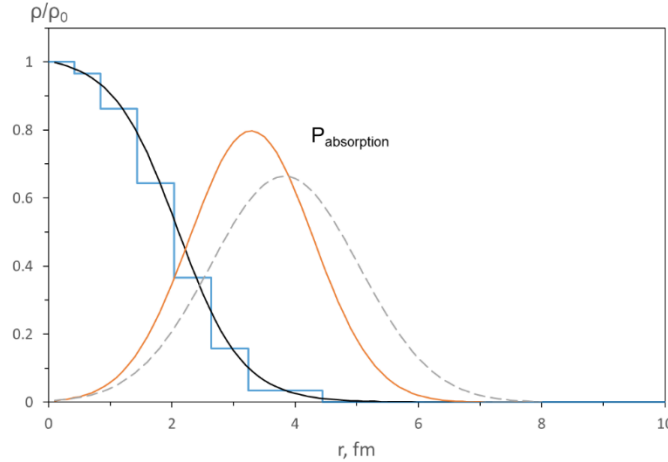


Figure 1. Left: The radial distribution of the relative density of protons and neutrons throughout the $^{12}_6C$ nucleus (they are identical). The solid black line is a Fermi density distribution, while the blue histogram is an approximation used to divide the nucleus into seven zones of constant density. Right: The radial dependence of the absorption probability P_{abs} for the $^{12}_6C$ nucleus is shown for an antineutron (solid) and an antiproton (dashed). Note that the eighth zone extends from the end of zone seven at $r = 4.44 fm$ to $r = 10 fm$.

2.2 Antineutron annihilation within the $^{40}_{18}Ar$ nucleus

The conversion of a bound neutron into an associated antineutron is significantly suppressed within the nuclear environment. The reason for this is the large difference between the values of the effective nuclear potential for the neutron and antineutron, along with the presence of annihilation channels for

the antineutron [4]. The question of the magnitude of the suppression of the $n \rightarrow \bar{n}$ transformation occurring within the nucleus has been the subject of in depth discussions between theoreticians for many years [15,16,17]. The $n \rightarrow \bar{n}$ transformation would be more probable for neutrons with lower binding energy. In addition, the maximum of the antineutron wave-function is located beyond the nuclear radius [18]. With regard to modeling the transformation in the ${}^{40}_{18}\text{Ar}$ nucleus, the difference between the absorption of the slow neutron by the ${}^{12}_6\text{C}$ nucleus, as discussed in the previous section, comes in the first stage only. For a reliable description of the absorption process of the antineutron produced by the $n \rightarrow \bar{n}$ transformation within ${}^{40}_{18}\text{Ar}$, it is necessary to determine the radial dependence of the probability density of the transformation within the nucleus. This calculation has recently been completed by colleagues, and we plan to include it in the model with a future co-publication. However, for a first approximation, the simulation outputs shown in *this* article are considered for the case when the transformation occurs with equal probability for all neutrons within the peripheral zone of the nucleus. As with the ${}^{12}_6\text{C}$ nucleus, the nucleon density distribution of the ${}^{40}_{18}\text{Ar}$ nucleus is described by expression (12) and is approximated as being divided into seven zones of constant density. In this first approximation, it is assumed that the neutrons are distributed throughout the nucleus identically to protons.

2.3 The nuclear model and nucleon momentum distribution

Within the INC model, the nucleus is considered to be a degenerate, free Fermi gas of nucleons, enclosed within a spherical potential well with a radius equal to the nuclear radius. Nucleons fill all energy levels of the potential well, from the lowest, when a nucleon can have the largest negative potential energy and zero momentum, to the highest echelons of the Fermi level, where the nucleon moves with Fermi momentum p_{FN} , and is retained within the nucleus only because of the binding energy ε (where $\varepsilon \approx 7 \text{ MeV}$ per nucleon). In the interval $p \in [0, p_{FN}]$, the three-momentum of the nucleon can take all permissible values with equal probability. The differential probability distribution of the nucleons with respect to the total momentum and kinetic energy [14] then takes the form:

$$W(p) = \frac{3p^2}{p_{FN}^3}, \quad p \leq p_{FN}, \quad (13)$$

$$W(T) = \frac{3T^{\frac{1}{2}}}{2T_{FN}^{\frac{3}{2}}}, \quad T \leq T_{FN}. \quad (14)$$

Here, T is the kinetic energy of a nucleon within the nucleus, and $T_{FN} = \frac{p_{FN}^2}{2m_N}$ represents the boundary Fermi kinetic energy, while m_N is the mass of the nucleon. If the nucleons are distributed evenly throughout the spherical well having a radius $R = r_0 A^{\frac{1}{3}}$ (and where r_0 is 1.2-1.4 fm), then their Fermi momentum and energy are easily expressed in terms of the radius. Because every cell in phase space $d^3x d^3p$ contains a number of states

$$\frac{2s + 1}{(2\pi\hbar)^3} d^3x d^3p \quad (15)$$

(s is the spin of the nucleon) and the total number of protons and neutrons in the nucleus being equal to n_N , it then follows from the normalization condition that

$$\frac{2s+1}{(2\pi\hbar)^3} \int d^3x d^3p = \frac{V p_{FN}^3}{3\pi^2 \hbar^3} = n_N, \quad (16)$$

and one finally gets that

$$p_{FN} = \hbar \left(\frac{3\pi^2 n_N}{V} \right)^{\frac{1}{3}}, \quad (17)$$

$$T_{FN} = \frac{p_{FN}^2}{2m_N} = \frac{\hbar^2}{2m_N} \left(\frac{3\pi^2 n_N}{V} \right)^{\frac{2}{3}}, \quad (18)$$

where $V = \frac{4}{3}\pi R^3$ is the volume of the nucleus, and m_N remains the nucleon mass.

If the nucleus is subdivided into concentric spherical zones of constant density, the values of p_{FN} and T_{FN} for each zone are calculated similarly to equations (17) and (18), but with an i -th radius, and the density of the nucleons within this i -th zone. Figure 2 shows the spatial distribution of the potential $V_N = -(T_{FN} + \varepsilon)$ for protons and neutrons in both $^{12}_6\text{C}$ and $^{40}_{18}\text{Ar}$ nuclei. The momentum distribution of the nucleons in individual zones will be the same as for a degenerate Fermi gas, and the probability of the nucleon to have momentum p in the i th-zone will continue to be determined by (13), although with the corresponding to i th-zone's boundary Fermi momentum value. Figure 3 shows the momentum distributions of nucleons for both $^{12}_6\text{C}$ and $^{40}_{18}\text{Ar}$ nuclei, obtained by summing all the momentum distributions for all individual zones. From Figures 2 and 3, we can see that the nucleons located in the central zone of the nucleus have the highest value of T_{FN} , and, accordingly, the maximum value of the Fermi momentum p_{FN} . Therefore, the contribution to the total momentum distribution from the nucleons located in the central ($i = 1$) zone gives the high-momentum part and extends up to 250 – 270 MeV/c . Conversely, the nucleons located within the peripheral zone of the nucleus ($i = 7$) have momenta up to 80 – 100 MeV/c . Moreover, the contribution to the overall momentum distribution of a particular zone is greater the more nucleons within it.

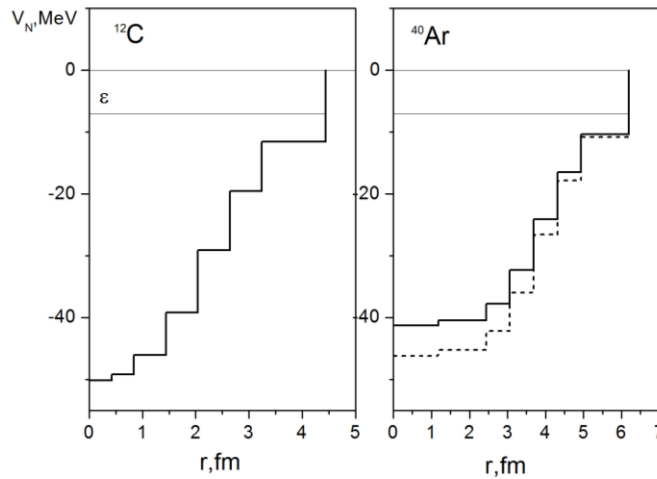


Figure 2: The spatial distribution of the potential $V_N = -(T_{FN} + \varepsilon)$, with appropriate partitioning of the nucleus into seven zones for protons (solid histogram) and neutrons (dotted histogram) for both $^{12}_6\text{C}$ and $^{40}_{18}\text{Ar}$ nuclei (for $^{12}_6\text{C}$, the solid and dotted histograms lay atop one another). ε is the average nuclear binding energy of 7 MeV per nucleon.

Thus, for $^{12}_6\text{C}$ nuclei in the first stage, the nucleons are distributed within the nucleus according to the step density function (see Figure 1). Next, according to the radial distribution of the antineutron absorption probability in the carbon nucleus $P_{abs}(r)$ (also Figure 1), the point of annihilation is taken randomly by Monte Carlo technique. The radius of this point determines the number of the zone in which the nucleon partner (neutron or proton) is located, with which the antineutron annihilates.

The physics underlying this transformation for an $^{40}_{18}\text{Ar}$ nucleus is different, since the antineutron generated from $n \rightarrow \bar{n}$ is not extranuclear in nature, but instead depends entirely on the magnitude of the intranuclear binding energy as a function of radius. Generally, it is thought that the bound transformation should occur near the surface of the nucleus (possibly even *outside* the nuclear envelope). Because the radial probability density function of the $n \rightarrow \bar{n}$ transformation has only recently been calculated for the case of an $^{40}_{18}\text{Ar}$ nucleus, at the current stage of model development discussed throughout this article, for an approximate comparison, any neutron from the peripheral zone of the nucleus is selected randomly. We assume that an antineutron resulting from the transformation has kinetic energy $T_{\bar{n}} = T_n + \varepsilon$, and annihilates on the nearest nucleon neighbor.

Further, the simulation is done within the same scheme for both $^{12}_6\text{C}$ and $^{40}_{18}\text{Ar}$ nuclei. The annihilation partner has Fermi momentum randomly selected from the momentum distribution for a particular zone; then, the annihilation occurs.

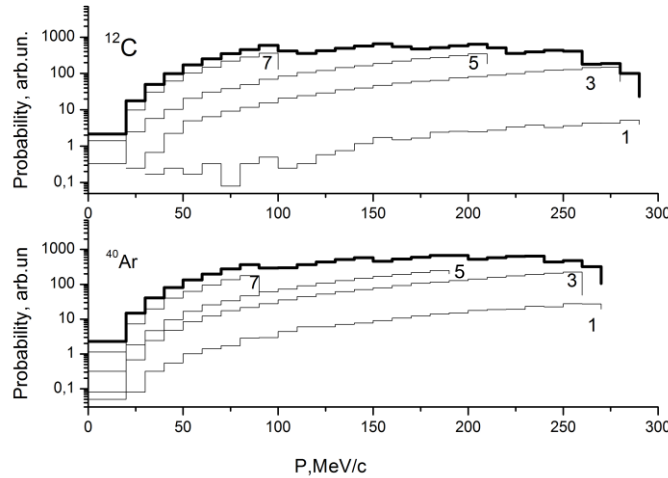


Figure 3. The thick histogram shows the momentum distribution of intranuclear nucleons in both $^{12}_6\text{C}$ and $^{40}_{18}\text{Ar}$ nuclei, summed over all zones. The thin lines show histograms which correspond to contributions from individual zones of the nucleus to the total momentum distribution (which shows contributions only from odd-numbered zones so that the picture is not indecipherable). The zone number i is shown at the right of each histogram. Note the logarithmic scale of probability.

2.4 Annihilation model

The phenomena of $\bar{N}N$ annihilation can lead to the creation of many particles through many possible (at times ~ 200) exclusive reaction channels; many neutral particles may be present, which can make experimental study difficult. Experimental information for exclusive channels is known only for a small fraction of possible annihilation channels, therefore a model has been created to describe the $\bar{N}N$ annihilation. A statistical model has been chosen based on $SU(3)$ symmetry [19]. Work to generalize the unitary-symmetric model for $\bar{N}N$ annihilations, along with the development of methods for calculating the characteristics of mesons produced from the annihilation, was performed by I. A. Pshenichnov [20].

According to the model, the $\bar{N}N$ annihilation allows for the production of between two to six intermediate particles. Given the estimates of the phase space volume at low momenta, the production of a larger number of intermediate particles is unlikely. Intermediate particles, such as π, η, ρ, ω and η mesons, are all possible; the channels with strangeness production are not considered within this version of the model. The unitary-symmetric statistical model predicts 106 $\bar{p}p$ annihilation channels, and 88 $\bar{p}n$ annihilation channels, but this differs from experiments, which effectively measure only ~ 40 channels for $\bar{p}p$ and ~ 10 channels for $\bar{p}n$ annihilation. However, neither the statistical model, nor the experimental data, can provide a complete *exclusive* description of the elementary annihilation processes. For this reason, *semi-empirical* Tables 1 and 2 of annihilation channels are employed for use in annihilation modeling. These are obtained as follows: First, all experimentally measured channels were included in Tables 1 & 2. Then, by using the isotopic relations, probabilities were found for those channels that have the same configurations but different particle charges. Finally, the predictions of the statistical model with $SU(3)$ symmetry were entered for the remaining intermediate channels. Sometimes the probabilities of intermediate channels measured in different experiments differ significantly. In this case, the data in the semi-empirical tables were corrected within experimental accuracies in order to describe the topological cross section for $\bar{p}p$ and $\bar{p}n$ in the best way possible. In our approach, the entire collection of experimental data was used: multi-particle topologies, inclusive spectra, topological pion cross sections, and branching ratios of various resonance channels. The following pages show the semi-empirical tables, with probabilities of various $\bar{p}p$ and $\bar{p}n$ annihilation channels included. In further modeling of $\bar{N}A$ interactions, it is considered that channels for $\bar{n}n$ are identical to $\bar{p}p$ channels, and that annihilation channels for $\bar{n}p$ are charge conjugated to $\bar{p}n$ channels. All experimental data used for comparison with this annihilation model are described in great detail in [21].

Channel	Probability (%)	Channel	Probability (%)	Channel	Probability (%)
$\eta\eta$	0.01 1)	$\eta\eta\pi^+\pi^-$	0.07	$\pi^+\pi^+\pi^+\pi^-\pi^-\pi^-$	2.83
$\eta\omega$	0.34 1)	$\eta\eta\pi^0\pi^0$	0.02	$\pi^+\pi^+\pi^-\pi^-\pi^0\pi^0$	9.76
$\omega\omega$	1.57 1)	$\eta\omega\pi^+\pi^-$	0.04	$\pi^+\pi^-\pi^0\pi^0\pi^0\pi^0$	2.68
$\pi^+\pi^-$	0.40 1)	$\eta\omega\pi^0\pi^0$	0.01	$\pi^0\pi^0\pi^0\pi^0\pi^0\pi^0$	0.07
$\pi^0\pi^0$	0.02 1)	$\pi^+\pi^-\pi^0\eta$	1.22	$\pi^+\pi^+\pi^+\pi^-\pi^-\rho^-$	0.02
$\pi^+\rho^-$	1.52 1)	$\pi^0\pi^0\pi^0\eta$	0.17	$\pi^+\pi^+\pi^-\pi^-\pi^-\rho^+$	0.02
$\pi^-\rho^+$	1.52 1)	$\pi^+\pi^-\pi^0\omega$	2.84	$\pi^+\pi^+\pi^-\pi^-\pi^0\rho^0$	0.06
$\pi^0\rho^0$	1.57 1)	$\pi^0\pi^0\pi^0\omega$	0.40	$\pi^+\pi^+\pi^-\pi^0\rho^-$	0.06
$\rho^-\rho^+$	3.37 2)	$\pi^+\pi^-\rho^0\eta$	0.06	$\pi^+\pi^-\pi^-\pi^0\rho^+$	0.06
$\rho^0\rho^0$	0.67 1)	$\pi^+\pi^0\rho^-\eta$	0.06	$\pi^+\pi^-\pi^0\pi^0\rho^0$	0.03
$\pi^0\eta$	0.06 1)	$\pi^-\pi^0\rho^+\eta$	0.06	$\pi^+\pi^0\pi^0\pi^0\rho^-$	0.01
$\pi^0\omega$	0.58 1)	$\pi^0\pi^0\rho^0\eta$	0.02	$\pi^-\pi^0\pi^0\pi^0\rho^+$	0.01
$\rho^0\eta$	0.90 1)	$\pi^+\pi^+\pi^-\pi^-$	2.74	$\pi^+\pi^+\pi^-\pi^-\pi^0\eta$	0.31
$\rho^0\omega$	0.79 1)	$\pi^+\pi^-\pi^0\pi^0$	3.89	$\pi^+\pi^-\pi^0\pi^0\pi^0\eta$	0.17
$\pi^+\pi^-\pi^0$	2.34 1)	$\pi^0\pi^0\pi^0\pi^0$	0.21	$\pi^0\pi^0\pi^0\pi^0\pi^0\eta$	0.01
$\pi^0\pi^0\pi^0$	1.12 1)	$\pi^+\pi^+\pi^-\rho^-$	2.58 1)	$\pi^+\pi^+\pi^-\pi^-\pi^0\omega$	0.10
$\pi^+\pi^-\rho^0$	2.02 1)	$\pi^+\pi^-\pi^-\rho^+$	2.58 1)	$\pi^+\pi^-\pi^0\pi^0\pi^0\omega$	0.06
$\pi^+\pi^0\rho^-$	2.02 2)	$\pi^+\pi^-\pi^0\rho^0$	6.29 1)	$\eta\eta\eta$	0.0036
$\pi^-\pi^0\rho^+$	2.02 2)	$\pi^+\pi^0\pi^0\rho^-$	5.05 2)	$\eta\eta\rho^0$	0.0002
$\pi^0\pi^0\rho^0$	1.01 2)	$\pi^-\pi^0\pi^0\rho^+$	5.05 2)	$\omega\omega\pi^+\pi^-$	0.0002
$\pi^+\rho^-\rho^0$	1.23	$\pi^0\pi^0\pi^0\rho^0$	0.77 2)	$\omega\rho^0\pi^+\pi^-$	0.0005
$\pi^-\rho^+\rho^0$	1.23	$\pi^+\pi^+\pi^-\pi^-\pi^0$	2.61	$\omega\rho^-\pi^+\pi^0$	0.0005
$\pi^0\rho^+\rho^-$	1.23	$\pi^+\pi^-\pi^0\pi^0\pi^0$	1.37	$\omega\rho^+\pi^-\pi^0$	0.0005
$\pi^0\rho^0\rho^0$	0.54	$\pi^0\pi^0\pi^0\pi^0\pi^0$	0.07	$\omega\rho^0\pi^0\pi^0$	0.0002
$\pi^+\pi^-\eta$	1.50 1)	$\pi^+\pi^+\pi^-\pi^-\rho^0$	0.08	$\rho^-\rho^-\pi^+\pi^+$	0.0003
$\pi^+\pi^-\omega$	3.03 1)	$\pi^+\pi^+\pi^-\pi^0\rho^-$	0.16	$\rho^0\rho^0\pi^0\pi^0$	0.0001
$\pi^0\pi^0\omega$	0.79 2)	$\pi^+\pi^-\pi^-\pi^0\rho^+$	0.16	$\rho^+\rho^-\pi^+\pi^-$	0.0011
$\pi^+\rho^-\eta$	0.84	$\pi^+\pi^-\pi^0\pi^0\rho^0$	0.12	$\rho^0\rho^0\pi^+\pi^-$	0.0004
$\pi^-\rho^+\eta$	0.84	$\pi^+\pi^0\pi^0\pi^0\rho^-$	0.04	$\rho^-\rho^0\pi^+\pi^0$	0.0008
$\pi^0\rho^0\eta$	0.44	$\pi^0\pi^0\pi^0\pi^0\rho^0$	0.01	$\rho^+\rho^+\pi^-\pi^-$	0.0003
$\pi^+\rho^-\omega$	1.10	$\pi^+\pi^+\pi^-\pi^-\eta$	0.11 1)	$\rho^+\rho^0\pi^-\pi^0$	0.0008
$\pi^-\rho^+\omega$	1.10	$\pi^+\pi^-\pi^0\pi^0\eta$	0.22 2)	$\rho^+\rho^-\pi^0\pi^0$	0.0004
$\pi^0\rho^0\omega$	0.57	$\pi^0\pi^0\pi^0\pi^0\eta$	0.01 2)	$\pi^+\pi^-\pi^0\eta\eta$	0.0055
$\eta\eta\pi^0$	0.11	$\pi^+\pi^+\pi^-\pi^-\omega$	1.80 1)	$\pi^0\pi^0\pi^0\eta\eta$	0.0007
$\eta\omega\pi^0$	0.30	$\pi^+\pi^-\pi^0\pi^0\omega$	2.58 2)		
$\omega\omega\pi^0$	0.37	$\pi^0\pi^0\pi^0\pi^0\omega$	0.10 2)		

Table 1. Probability of intermediate states for $\bar{p}p$ annihilation (%). Note that 1) indicates a probability attained from experiment; see references used in [21]. Note that 2) indicates that the probabilities are obtained from isotopic relations. The sum of all branching ratios is normalized to 100 percent.

Channel	Probability (%)	Channel	Probability (%)	Channel	Probability (%)
$\pi^- \pi^0$	0.49 1)	$\pi^+ \pi^- \pi^- \omega$	10.52 1)	$\pi^+ \pi^+ \pi^- \pi^- \pi^0 \rho^-$	0.07
$\pi^- \omega$	0.48 1)	$\pi^- \pi^0 \pi^0 \omega$	7.01 2)	$\pi^+ \pi^- \pi^- \pi^- \pi^0 \rho^+$	0.05
$\pi^- \rho^0$	0.47 1)	$\pi^+ \pi^- \rho^- \eta$	0.08	$\pi^+ \pi^- \pi^- \pi^0 \pi^0 \rho^0$	0.06
$\pi^0 \rho^-$	0.47 2)	$\pi^- \pi^- \rho^+ \eta$	0.05	$\pi^+ \pi^- \pi^0 \pi^0 \pi^0 \rho^-$	0.03
$\rho^- \rho^0$	3.51 2)	$\pi^- \pi^0 \rho^0 \eta$	0.06	$\pi^- \pi^- \pi^0 \pi^0 \pi^0 \rho^+$	0.02
$\pi^- \eta$	0.29 1)	$\pi^0 \pi^0 \rho^- \eta$	0.02	$\pi^- \pi^0 \pi^0 \pi^0 \pi^0 \rho^0$	0.01
$\rho^- \eta$	2.27	$\pi^+ \pi^- \pi^- \pi^0$	5.51	$\pi^+ \pi^+ \pi^- \pi^- \pi^- \eta$	0.14
$\rho^- \omega$	3.51 2)	$\pi^- \pi^0 \pi^0 \pi^0$	1.38	$\pi^+ \pi^- \pi^- \pi^0 \pi^0 \eta$	0.30
$\pi^+ \pi^- \pi^-$	2.86	$\pi^+ \pi^- \pi^- \rho^0$	0.99	$\pi^- \pi^0 \pi^0 \pi^0 \pi^0 \eta$	0.05
$\pi^- \pi^0 \pi^0$	1.90	$\pi^+ \pi^- \pi^0 \rho^-$	1.97	$\pi^+ \pi^+ \pi^- \pi^- \pi^- \omega$	0.05
$\pi^+ \pi^- \rho^-$	3.62 1)	$\pi^- \pi^- \pi^0 \rho^+$	0.99	$\pi^+ \pi^- \pi^- \pi^0 \pi^0 \omega$	0.09
$\pi^- \pi^- \rho^+$	0.58 1)	$\pi^- \pi^0 \pi^0 \rho^0$	0.75	$\pi^- \pi^0 \pi^0 \pi^0 \pi^0 \omega$	0.01
$\pi^- \pi^0 \rho^0$	5.61 2)	$\pi^0 \pi^0 \pi^0 \rho^-$	0.25	$\eta \eta \rho^-$	0.0003
$\pi^0 \pi^0 \rho^-$	3.51 2)	$\pi^+ \pi^+ \pi^- \pi^- \pi^-$	1.24	$\omega \omega \pi^- \pi^0$	0.0002
$\pi^+ \rho^- \rho^-$	1.04	$\pi^+ \pi^- \pi^- \pi^0 \pi^0$	2.72	$\omega \rho^- \pi^+ \pi^-$	0.0008
$\pi^- \rho^+ \rho^-$	2.09	$\pi^- \pi^0 \pi^0 \pi^0 \pi^0$	0.37	$\omega \rho^+ \pi^- \pi^-$	0.0004
$\pi^- \rho^0 \rho^0$	0.70	$\pi^+ \pi^+ \pi^- \pi^- \rho^-$	0.12	$\omega \rho^0 \pi^- \pi^0$	0.0005
$\pi^0 \rho^- \rho^0$	1.39	$\pi^+ \pi^- \pi^- \pi^- \rho^+$	0.08	$\omega \rho^- \pi^0 \pi^0$	0.0003
$\pi^- \pi^0 \eta$	1.23	$\pi^+ \pi^- \pi^- \pi^0 \rho^0$	0.16	$\rho^- \rho^0 \pi^+ \pi^-$	0.0011
$\pi^- \pi^0 \omega$	5.05	$\pi^+ \pi^- \pi^0 \pi^0 \rho^-$	0.16	$\rho^- \rho^- \pi^+ \pi^0$	0.0005
$\pi^0 \rho^- \eta$	0.78	$\pi^- \pi^- \pi^0 \pi^0 \rho^+$	0.08	$\rho^+ \rho^0 \pi^- \pi^-$	0.0005
$\pi^- \rho^0 \eta$	0.78	$\pi^- \pi^0 \pi^0 \pi^0 \rho^0$	0.05	$\rho^- \rho^+ \pi^0 \pi^-$	0.0011
$\pi^- \rho^0 \omega$	1.03	$\pi^0 \pi^0 \pi^0 \pi^0 \rho^-$	0.01	$\rho^0 \rho^0 \pi^0 \pi^-$	0.0004
$\pi^0 \rho^- \omega$	1.03	$\pi^+ \pi^- \pi^- \pi^0 \eta$	0.37	$\rho^- \rho^0 \pi^0 \pi^0$	0.0004
$\eta \eta \pi^-$	0.21	$\pi^- \pi^0 \pi^0 \pi^0 \eta$	0.09	$\pi^+ \pi^- \pi^- \eta \eta$	0.0042
$\pi^- \omega \eta$	0.60	$\pi^+ \pi^- \pi^- \pi^0 \omega$	0.40	$\pi^- \pi^0 \pi^0 \eta \eta$	0.0028
$\pi^- \omega \omega$	0.71	$\pi^- \pi^0 \pi^0 \pi^0 \omega$	0.09		
$\eta \eta \pi^- \pi^0$	0.06	$\pi^+ \pi^+ \pi^- \pi^- \pi^- \pi^0$	8.33		
$\eta \omega \pi^- \pi^0$	0.03	$\pi^+ \pi^+ \pi^- \pi^- \pi^- \pi^0$	6.67		
$\pi^+ \pi^- \pi^- \eta$	1.00	$\pi^- \pi^0 \pi^0 \pi^0 \pi^0 \pi^0$	0.56		
$\pi^- \pi^0 \pi^0 \eta$	0.67	$\pi^+ \pi^+ \pi^- \pi^- \pi^- \rho^0$	0.02		

Table 2. Probability of intermediate states for $\bar{p}n$ annihilation (%). Similarly note that 1) indicates a probability attained from experiment; see references used in [21]. Note that 2) indicates that the probabilities are obtained from isotopic relations. The sum of all branching ratios is normalized to 100 percent.

Considering the laws of energy and momentum conservation for each annihilation, the procedure for simulating the characteristics of both the intermediate particles and their various decay products consists of the following: first, a single channel from the table is randomly selected via Monte Carlo technique as the initial state, with all necessary momenta of all annihilation particles determined

according to the pertinent phase-space volume. This takes into account the Breit-Wigner mass distribution for meson resonances, while all pions have a mass value of $0.14 \frac{GeV}{c^2}$. The subsequent disintegration of unstable mesons is modeled according to experimentally known branching ratios. All major decay modes for meson resonances have been considered, such as in Table 3.

Channel	Probability (%)	Channel	Probability (%)	Channel	Probability (%)
$\eta \rightarrow 2\gamma$	39.3	$\omega \rightarrow \pi^+\pi^-\pi^0$	89.0	$\rho^+ \rightarrow \pi^+\pi^0$	100
$\eta \rightarrow 3\pi^0$	32.1	$\omega \rightarrow \pi^0\gamma$	8.7	$\rho^- \rightarrow \pi^-\pi^0$	100
$\eta \rightarrow \pi^+\pi^-\pi^0$	23.7	$\omega \rightarrow \pi^+\pi^-$	2.3	$\rho^0 \rightarrow \pi^+\pi^-$	100
$\eta \rightarrow \pi^+\pi^-\gamma$	4.9				

Table 3. Pertinent decay branching ratios of intermediate resonance particles shown in %. All channels have been determined experimentally.

Table 4 shows the average multiplicity of mesons formed in $\bar{p}p$ annihilations at rest. The simulation results are within the range of experimental uncertainties. From these simulation results, it follows that more than 35% of all pions have been formed by the decay of meson resonances. Figure 4 shows the pion multiplicity distribution generated by $\bar{p}p$ annihilation, while Figure 5 shows the charged pion momentum distribution. From considering Table 4 and Figures 4 and 5, it follows that the Monte Carlo and available experimental data are in general agreement with the main features of $\bar{p}p$ annihilation at rest.

	Simulated $\bar{p}p$	Experimental $\bar{p}p$
$M(\pi)$	4.910	4.98±0.35 [22] 4.94±0.14 [23]
$M(\pi^\pm)$	3.110	3.14±0.28 [22] 3.05±0.04 [22] 3.04±0.08 [23]
$M(\pi^0)$	1.800	1.83±0.21 [22] 1.93±0.12 [22] 1.90±0.12 [23]
$M(\eta)$	0.091	0.10±0.09 [24] 0.0698±0.0079[22]
$M(\omega)$	0.205	0.28±0.16, [24] 0.22±0.01 [25]
$M(\rho^+)$	0.189	---
$M(\rho^-)$	0.191	---
$M(\rho^0)$	0.193	0.26±0.01 [25]
$M(\pi^-)_{dec}$	1.908	---
$M(\pi^+)_{dec}$	0.606	---
$M(\pi^-)_{dec}$	0.606	---
$M(\pi^0)_{dec}$	0.695	---

Table 4. Meson multiplicities for simulated and experimental $\bar{p}p$ annihilations, shown in absolute particle counts.

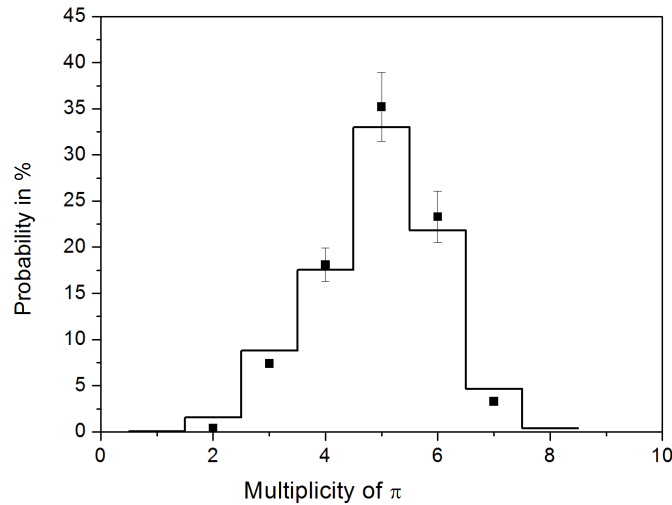


Figure 4. The pion multiplicity distribution for $\bar{p}p$ annihilation at rest (taking into account the decay of meson resonances). The solid histogram shows the model, with the points showing experimental data [22].

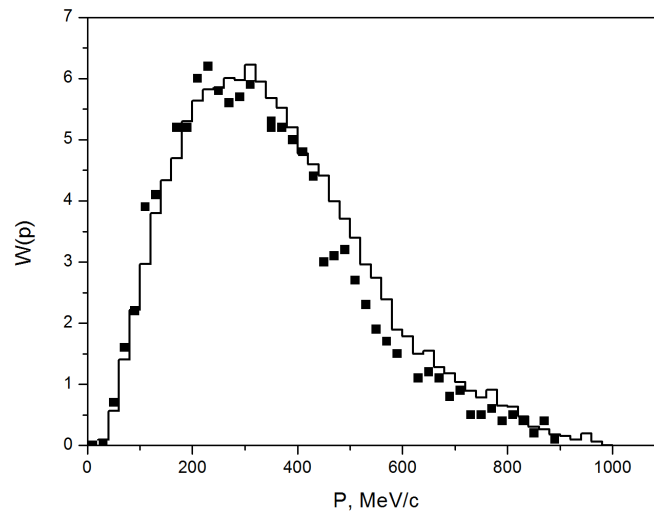


Figure 5. The momentum distribution of charged pions produced in $\bar{p}p$ annihilation at rest (taking into account the decay of meson resonances). The solid histogram shows the model, with the points showing experimental data [26].

2.5 Intranuclear Cascade (INC) Model

Inelastic nuclear interactions are clearly statistical in nature, as they can be realized in many possible states. The statistical approach is key to describing such systems, and replaces the evolution of a system's wave function with the description of the evolution of an ensemble of the many possible states of the system. There are two dramatically different stages of a deeply inelastic interaction: (1) a fast, out-of-equilibrium stage in which energy is redistributed between the various degrees of freedom within the nucleus as a finite open system, and (2) the slow equilibrium stage of the decay of the thermalized residual nuclei.

The Intranuclear Cascade (INC) Model is a phenomenological model describing the out-of-equilibrium stage of inelastic interactions and operates with the notion of the probability of a nuclear system being in a given state. Transitions between different states are caused by two-body interactions, which lead to

secondary particles exiting the nucleus, dissipating the excitation energy in the process. However, this phenomenological model is linked to fundamental microscopic theory. It was shown in [27] that it is possible to transform a non-stationary Schrödinger equation for a many body system into kinetic equations, if large energy (and so short time) wave packet formulations are used. To explain, if the duration of the wave packet's individual collisions are shorter than the interval of time between consecutive collisions, then the amplitudes of these collisions will not interfere. This condition is essentially analogous to the condition of a free gas approximation: $\tau_0 < \tau_{FP}$, where τ_0 is the duration time of the collision, and τ_{FP} is the mean-free-path time. This condition allows for the consideration of a particle's motion as in a dilute gas, like independent motion on free path trajectories perturbed by binary collisions. Under these conditions, in a quasi-classical way, one can use the local momentum approximation by assigning a particle a momentum $\vec{P}(\vec{r})$ between consecutive collisions. In this case, the quantum kinetic equation is transformed into kinetic equation of a Boltzmann-type describing the transport of particles within nuclear media; this differs from the conventional Boltzmann equation only by accounting for the Pauli exclusion principle. Thus, the INC model is a numerical solution of the quasi-classical kinetic equation of motion for a multi-particle distribution function using the Monte Carlo method.

We will now focus our discussion on the scope of the INC model and the possibility of generalizing its use, such as in the event of the absorption of a slow antineutron. The principles underlying the model are altogether justified if the following conditions are met [14,27,28]:

- a) The wavelengths, λ , of the majority of moving particles are less than the mean distance between nucleons within the nucleus, i.e. $\lambda < \Delta$, where $\Delta \approx \left[\frac{4\pi R^3}{3A} \right]^{\frac{1}{3}} \approx r_0 \approx 1.3 \text{ fm}$. In this case, the system acquires quasi-classical characteristics, and one can speak of the trajectories of particles and two-body interactions within the nucleus. For individual nucleons, this corresponds to an energy of more than tens of MeV . Of course, this condition cannot be met in the case of a slow antineutron, therefore, its absorption is described in the framework of the optical model.
- b) From the interaction time $\tau_{Int} \approx \frac{r_N}{c} \approx 10^{-23} \text{ s}$, it must follow $\tau_{Int} \leq \tau_{FP}$, where the mean-free-path-length time is $\tau_{FP} = \frac{l}{c} = \frac{1}{\rho\sigma c} \approx \frac{4\pi R^3}{3A\sigma c} \approx \frac{3 \times 10^{-22}}{\sigma} \text{ s}$ (and where σ is the cross section in mB). This requirement is equivalent to the condition of requiring sufficiently small cross sections of elementary interactions, and proves problematic for pions produced from the annihilation and lying within the energy range of the Δ -resonance, where $\sigma > 100 \text{ mB}$. However, it should be kept in mind that the effective mean-free-path-length within the nucleus is *increased* by the Pauli exclusion principle; secondarily, because the uptake of the antineutron is on the periphery of the nucleus, where the nuclear density is low and the distance between the nucleons large, one can expect that the INC model would work in this case. Never-the-less, the comparison of the simulation results with experimental data is the main criterion for the applicability of the model.

The standard INC model is based on a numerical solution of the kinetic equation using a linearized approximation, which implies that the density of the media *does not change* in the development of the cascade, i.e. $N_c \ll A_t$ (where N_c is the number of cascading particles, and A_t is the number of nucleons making up the target nucleus). Such an approximation is violated in the case of multi-pion production in pA and πA interactions at $E_{p,\pi} \geq 3 - 5 \text{ GeV}$, and also in the case of annihilation,

especially when considering light nuclei such as $^{12}_6\text{C}$. A version of the model, which takes into account the effect of a local reduction in nuclear density, was first proposed in [28]. This version of the model considers the nucleus as consisting of separate nucleons, the position of their centers computed by Monte Carlo method according to the prescribed density distribution $\rho(R)$ such that the distance between their centers is no less than $2r_c$, where $r_c = 0.4 \text{ fm}$ is the nucleon core radius. A cascading particle may interact with any intranuclear nucleon which lies inside the cylinder of diameter $2r_{int} + \lambda$ extending along the particle's velocity vector (here, $r_{int} = \sqrt{\sigma/31.4}$ is the radius depending on the cross section σ , while λ is the deBroglie wavelength of the particle). The diameter of the cylinder is a parameter of the model and is chosen for better agreement with the experimental data. The key point to understand here is the ability to determine the probability of the cascading particle interacting with another constituent nucleon. We now consider this process in more detail.

Within the standard cascade model, the randomly chosen interaction point is computed from a Poisson distribution for the mean-free-path-length. In this case, the probability $\omega(k)$ of the particle experiencing k collisions along the path-length L in media with density ρ , where the particle has a total cross section σ , is defined as:

$$\omega(k) = e^{-\rho\sigma L} \frac{(\rho\sigma L)^k}{k!}. \quad (19)$$

If on the path-length L there lie n individual particle centers, each has an equal collision probability p for the particle to collide on k of n centers. This probability is described by a binomial distribution:

$$\omega(k, n, p) = \frac{n!}{k!(n-k)!} p^k q^{n-k}. \quad (20)$$

From the Poisson distribution (19), it follows directly that the probability of a particle experiencing *no collisions* along L is simply:

$$\omega(0) = e^{-\rho\sigma L}. \quad (21)$$

The same probability for this process can be obtained from the binomial distribution in (20), and is equal to:

$$\omega(0, n, p) = (1 - p)^n = q^n. \quad (22)$$

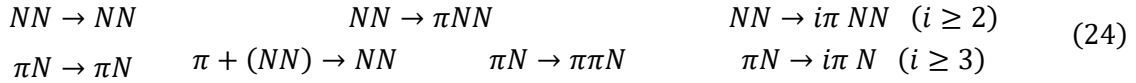
If one takes $\omega(0) = \omega(0, n, p)$, and when considering that $n = \rho\pi L(r_{int} + \lambda/2)^2$, then:

$$q = 1 - p = \exp[-\rho\sigma L/n] = \exp[-\sigma/\pi(r_{int} + \lambda/2)^2]. \quad (23)$$

An essential feature of the INC model is the fact that after interactions occur inside the nucleus, nucleons are considered as cascade particles, rather than constituent parts of the nuclear system. It is obvious that with a large multiplicity of cascade particles, fast particles pass through nuclear matter of higher density. In order to describe the evolution of the cascade and the decays of unstable meson resonances over time, an explicit time-coordinate has been incorporated into the model.

So, one can summarize the physical considerations that underlie the INC model:

- The nuclear target is a degenerate Fermi gas of protons and neutrons within a spherical potential well with a diffuse nuclear boundary. The real nuclear potentials for nucleons (V_N), antinucleons ($V_{\bar{N}}$), and mesons (V_π, V_η, V_ω) effectively takes into account the influence on the particle of all intranuclear nucleons. The depth of the potential well for the antinucleon and mesons within the nucleus remains a free-parameter of the model. Recognizing that the annihilation process usually occurs on the periphery of the nucleus, a good approximation for this is considered to be $V_{\bar{N}} \approx 0$ and $V_{mes} \approx 0$. In the future, a detailed study is planned to focus on the influence of the potentials on the simulation output.
- Hadrons involved in collisions are treated as classical particles. A hadron can initiate a cascade of consecutive, independent collisions upon nucleons within the target nucleus. The interactions between cascading particles are not taken into account.
- The cross sections of hadron-nucleon interactions are considered within the nucleus to be identical to those in vacuum, except that Pauli's exclusion principle explicitly prohibits transitions of cascade nucleons into states already occupied by other nucleons.



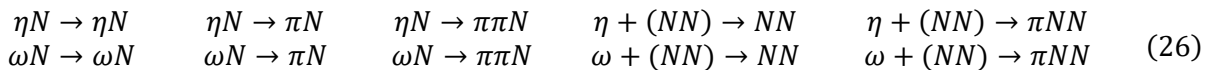
Elementary processes, such as those seen in the channels (24) shown above, are described by empirical approximations from analysis of experimental data on NN and πN interactions at kinetic energies $T < 20 GeV$ [14,28]

Now consider some of the features of the INC model related to the introduction of unstable meson resonances into the model. Modeling annihilation with meson resonances (i.e. $\bar{N}N \rightarrow i\pi + j\rho + k\eta + l\omega$) was described in the preceding section. It is assumed within the model that ρ -mesons produced by annihilation decay quickly enough to avoid interacting with any intranuclear nucleons. In contrast, ω -mesons produced by annihilation can both interact with other intranuclear nucleons *and* decay within or outside the nucleus. The competition between the decay of the ω -meson and its interaction with intranuclear nucleons is determined by the expression for the mean-free-path:

$$\frac{1}{\lambda} = \frac{1}{\lambda_{dec}} + \frac{1}{\lambda_{int}}, \quad (25)$$

where $\lambda_{int} = (\rho_n \sigma_{\omega N}^{tot})^{-1}$, $\lambda_{dec} = \gamma \beta (h\Gamma_\omega)^{-1}$, ρ_n is the nuclear density, and γ is the Lorentz factor. The mean lifetime of the η -meson is large enough for the particle to be considered stable within the nucleus, which can then decay upon exit. The model uses the experimentally measured decay modes of the meson resonances described above. When the annihilation products are allowed to disintegrate, their three-body decay is simulated by evaluation of the permissible phase-space volume.

To accommodate the passage of η -and- ω -mesons through nuclear material, in addition to channels listed in (24), the following interactions are also considered:



Along with the creation of η -and- ω -mesons by annihilation, the model also accounts for the creation of mesons through interactions between annihilation pions and nucleons, such as



For cross sections of reactions in (26), estimates given in [21] were employed. For those few reactions shown in (27), experimental cross sections were taken from compilation [29]. As these interactions are considered at relatively low energy, the angular distributions for reactions shown in (26) and (27) are assumed to be isotropic in the center of mass of the system. Reactions with three particles in the final state are simulated via their pertinent phase-space volume.

2.6 De-excitation of the residual nucleus

For inelastic nuclear reactions, after the rapid stage of the intranuclear cascade ($\tau_{cas} \simeq \tau_0$) and once statistical equilibrium ($\tau_{eq} \cong (5 - 10)\tau_0$) is established inside the residual nucleus, a slow stage begins ($\tau_{ev} \gg \tau_0$) involving the disintegration of the highly excited residual nucleus (note that $\tau_0 \leq 10^{-22}s$, which is the average time required for a particle to pass completely through the nucleus). The INC model is also able to describe the dissipation of energy throughout the nucleus. At the end of the cascade stage, the nuclear degenerate Fermi gas contains a number of "holes" N_h , which is equal to the number of collisions of cascade particles with nucleons within the nucleus. Also, there exists some number of excited particles N_p , which is equal to the number of slow cascade nucleons trapped by the nuclear potential well. The excitation energy of the residual nucleus E^* , is the sum of the energy of all such quasiparticles calculated from the Fermi energies ε_i :

$$E^* = \sum_{i=1}^{N_h} \varepsilon_i^h + \sum_{j=1}^{N_p} \varepsilon_j^p. \quad (28)$$

The resulting residual nuclei have a broad distribution of excitation energies E^* , momenta, masses, and charges. The INC model correctly accounts for the fluctuations of the cascade particles, and reliably defines the entire set of characteristics for residual nuclei.

The de-excitation mechanism for a residual nucleus is determined from the accumulated excitation energy of the nucleus [30]. Under low excitation energies (where $E^* \leq 2 - 3 \text{ MeV/nucl}$), the primary de-excitation mechanism is the consecutive emission (evaporation) of particles from the compound nucleus [31]. When the excitation energy of the nucleus is approaching the total binding energy (where $E^* \geq 5 \frac{\text{MeV}}{\text{nucl}}$), the prevalent mechanism is explosive decay [32]. For intermediate energies, both mechanisms coexist.

3. Comparison with experiment

The optical-cascade model described throughout this work has been used to analyze experimental data taken from the antiproton annihilation at rest on $^{12}_6\text{C}$ target nuclei. Table 5 shows the average multiplicity of emitted pions and protons. Experimental data on average pion multiplicities (values of which are shown at the bottom of the $\bar{p}\text{C}$ row) are taken from [23]. The final column of the table indicates the average energy of pions and photons (resulting from the decay of η -and- ω -mesons) emitted from the nucleus. Calculated values for the average multiplicities of pions (values of which are shown at the top of the $\bar{p}\text{C}$ row) are within accuracies of the experimental data. Since the antiproton primarily annihilates on the surface of the nucleus, most of the mesons produced fly out of the nucleus *without* any interaction. In the case of a light nucleus such as carbon, the effect of absorption of annihilation mesons is not large and the average multiplicity of pions emitted appear to be quite similar to the multiplicity of pions in $\bar{p}p$ annihilation (4.910). For comparison, Table 5 also shows results which

simulate the annihilation of a slow antineutron on a carbon nucleus. The comparison shows that the average pion multiplicity for an $\bar{n}C$ annihilation is somewhat *lower*, and that the average multiplicity for exiting nucleons slightly *higher* than the case of a stopped antiproton. This is due to the fact that the antineutron penetrates more deeply into the nucleus (seen in the solid line shown in Figure 1) compared to an antiproton (seen in the dashed line shown in Figure 1), and so there are more intranuclear interactions between annihilation mesons and constituent nucleons. Thus, the number of mesons emitted from the nucleus and their total energy E_{tot} are *reduced*, while instead the number of nucleons that kicked from the original nucleus during the fast cascading stage, and then emitted from the nucleus during the de-excitation process, is *increased*. In the case of peripheral annihilation of an antineutron on $^{40}_{18}Ar$, the pions are almost entirely free to leave the nucleus, increasing the value of E_{tot} , and so the number of emitted nucleons is significantly lower than $\bar{n}C$ annihilation. Note here that the calculation completed for $^{40}_{18}Ar$ is made in a *very rough* approximation with respect to the annihilation radius; this property requires further detailed investigation.

	Type	M_{π}	M_{π^+}	M_{π^-}	M_{π^0}	M_p	M_n	$E_{tot} (MeV)$
$\bar{p}C$	calculation	4.557	1.208	1.634	1.715	1.138	1.209	1736
	experiment	4.57 ± 0.15	1.25 ± 0.06	1.59 ± 0.09	1.73 ± 0.10	---	---	1758 ± 59
$\bar{n}C$	calculation	4.451	1.558	1.182	1.712	1.543	1.317	1679
$\bar{n}Ar$	calculation	4.599	1.651	1.267	1.680	0.727	0.804	1751

Table 5. The average outgoing particle multiplicities emitted after $\bar{p}C$, $\bar{n}C$ and $\bar{n}Ar$ annihilation and all decays. Experimental data taken from [23] is used as a comparison for $\bar{p}C$. In the first row (calculation for $\bar{p}C$), an option of the model with the antineutron potential was used.

Now, consider and compare the Monte Carlo calculation to other available experimental data and features for $\bar{p}C$ annihilation at rest. Figure 6 shows the charged pion multiplicity distribution emitted from the nucleus due to $\bar{p}C$ annihilation (shown as the solid histogram with points), $\bar{n}C$ (shown as the dotted histogram), and $\bar{n}Ar$ (the dashed histogram). As was expected, the differences in these distributions, as with the mean number of emitted pions, are not significant, although there appears to be some bias towards a smaller number of pions for $\bar{n}C$ and a larger number for $\bar{n}Ar$.

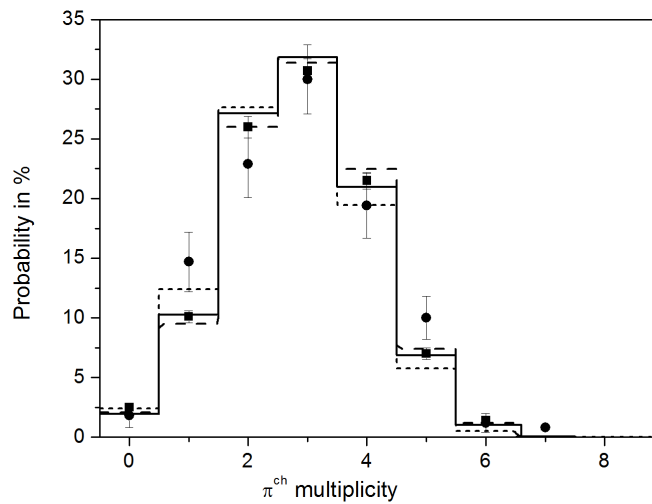


Figure 6. The probability (%) of formation of a given number of charged pions in antinucleon-nuclei annihilation. The solid histogram shows $\bar{p}C$. Experimental data: circles-[33], squares-[34]. The dotted histogram shows an $\bar{n}C$ calculation; the dashed histogram shows an $\bar{n}Ar$ calculation.

Figure 7 shows the distribution by number of events with the charge Q carried out by pions. For the $\bar{p}C$ annihilation the maxima of the distribution are $Q = -1$ and $Q = 0$, which practically corresponds to mesons exiting the nucleus without any interaction with nucleons. The optical-cascade model demonstrates good agreement with the experimental data. In the case of an annihilation with an \bar{n} , the distribution has a maximum Q that is shifted to $Q = 0$ and $Q = +1$, respectively. In the case of a peripheral annihilation for $\bar{n}Ar$, the distribution has a narrower maximum than $\bar{n}C$.

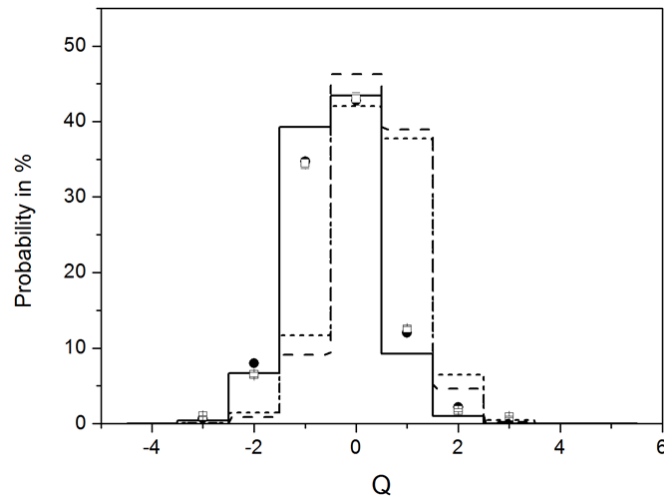


Figure 7. The probability (%) of particular values of total charge Q carried out by pions emitted from the nucleus. The solid histogram shows a $\bar{p}C$ calculation. Experimental data: open squares-[35], circles-[36]. The dotted histogram shows an $\bar{n}C$ simulation, while the dashed histogram shows an $\bar{n}Ar$ simulation.

Figure 8 shows the distribution of the number of emitted protons. The analysis of experimental data and simulation results show that a significant number of events (from $\sim 40\%$ for $\bar{n}C$, to $\sim 60\%$ for $\bar{n}Ar$) do not have *any* exiting protons.

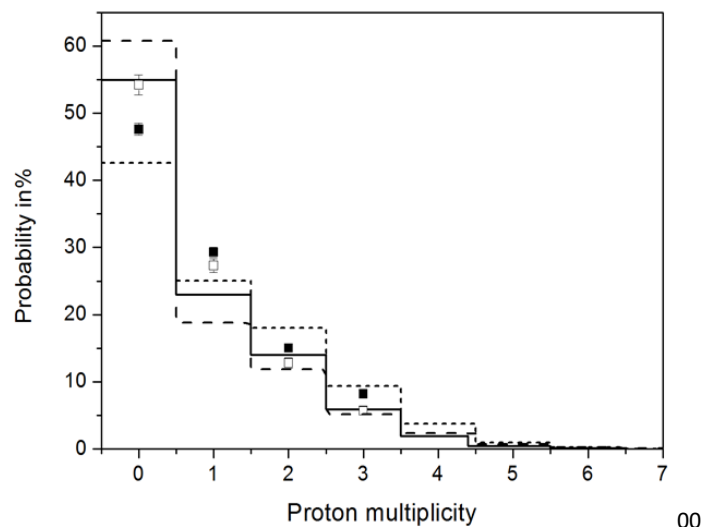


Figure 8. The probability (%) of the events with the given number of exiting protons. The solid histogram shows a $\bar{p}C$ calculation. Experimental data: solid squares-[34], open squares-[35]. The dotted histogram shows an $\bar{n}C$ calculation. The dashed histogram shows an $\bar{n}Ar$ calculation.

Figure 9 shows the momentum distribution for π^+ exiting the nucleus, which is rather similar to the momentum distribution of pions created by $\bar{p}p$ annihilation (as seen in Figure 5). To understand the uncertainty of the model, calculations were done 1) without any nuclear potential for the antineutron, and, as an option, 2) with a model where the antineutron nuclear potential is introduced similar to [21]. For mesons propagating inside the nucleus, we have not assumed any nuclear potentials. For Figures 11-18 in the following pages, option 1) is used. Both model calculations are presented in Figure 9, and show rather good agreement with experimental data, although there is some exaggerated absorption behavior corresponding to the Δ -resonance region ($\sim 260 \frac{MeV}{c}$). The difference between experimental measurements appears to be of the same order as the uncertainty in the calculation. Never-the-less, in the near future, we plan to study this question in more detail.

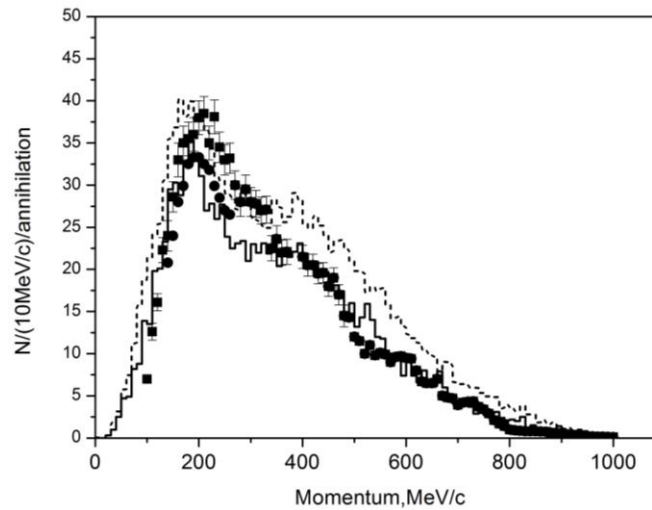


Figure 9. The π^+ momentum distribution is shown for antiproton annihilation at rest on carbon nuclei. The points show experimental data from [23,37]. The histograms show calculations, where the solid line shows an option of the model with a nuclear potential for the antineutron, and the dashed line is the calculation done without this potential. The nuclear potential for annihilation mesons inside the nucleus is assumed to be zero.

Figure 10 shows the energy spectrum of protons exiting the nucleus from $\bar{p}C$ annihilation at rest. In the low energy regime (up to $50 MeV$), evaporative protons provide a significant contribution to the spectrum. The model again shows good agreement with the available experimental data.

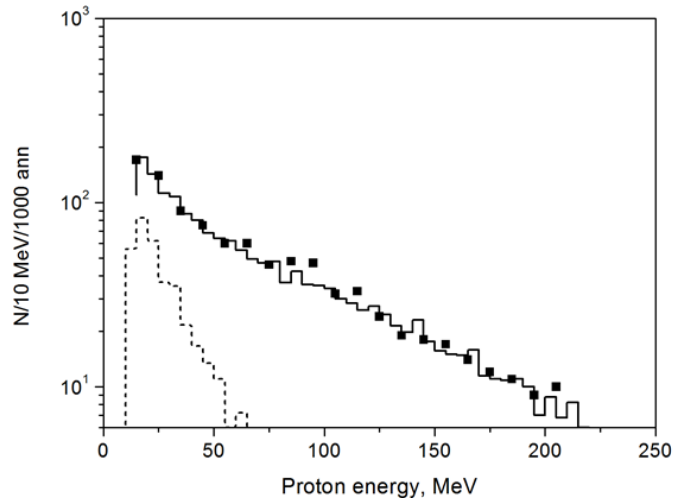


Figure 10. The exiting proton kinetic energy spectrum due to antiproton annihilation at rest on carbon nuclei. The solid histogram shows the simulation result. The dotted histogram shows the contribution which evaporative protons impart to the whole distribution. The points show the experimental data taken in [38].

From the comparisons made above between the simulation results of the optical-cascade model and experimental data of $\bar{p}C$ annihilation at rest, it follows that the model as a whole describes experiments well, thus accurately reflecting the dynamics of the annihilation process and the propagation of annihilation mesons throughout the nucleus.

4. $\bar{n}C$ Annihilation generator validation

Colleagues within the ESS $n \rightarrow \bar{n}$ collaboration have tested the model through its corresponding event generator comprehensively. The event generator outputs an annihilation point, annihilation product particle identities, energies, momenta, etc. These particles and variables as outputs are tracked and saved to file in three successive stages: 1) after the primary annihilation, 2) after all cascading ($n, p, \pi, \rho, \eta, \omega$) and evaporation particles have left the nucleus, and 3) after all decays of the meson resonances emitted from the nucleus (ρ, η, ω) are modeled.

As discussed in previous sections, multiplicity, charge, momentum and energy distributions of particles show good agreement with antiproton annihilation experimental data, and all simulated variables quantitatively satisfy the fundamental tenets of the required physics. Specifically, the generator has been shown to conserve charge, energy, momentum, baryon number, etc., through all three stages of simulation.

The output file type is .txt, and formatted in such a way as to easily separate the particle content and their respective physical variables through the stages. Analysis of the output has been completed by ESS colleagues using C++ and the CERN ROOT 6.10 modular scientific software framework [39]. 100,000 simulated events of $\bar{n}C$ annihilation events are available upon request from the authors. The currently available event files and the following plots are created only from the completed simulation file data without either antineutron or meson potentials. As several first tests of the generator, Figures 6-8 are here reproduced below, in order, directly from the $\bar{n}C$ annihilation simulation output file; some of the original figures already include the plots that will be shown in this section, but they are placed here for completion, and for future comparisons with the possible end user in mind.

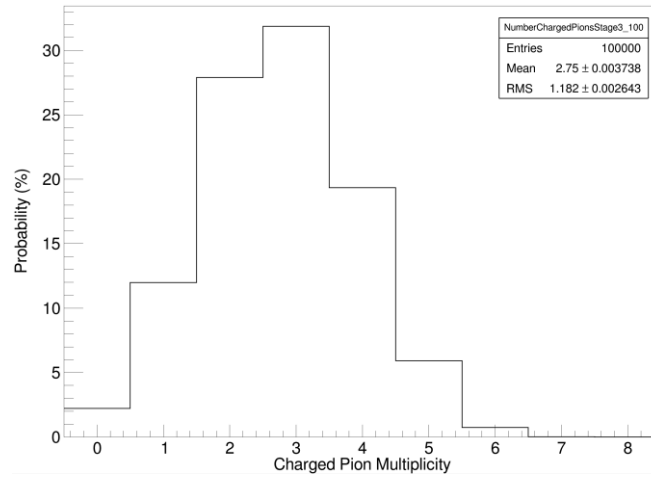


Figure 11. Reproduction of previous Figure 6 with $\bar{n}C$ generator. The probability of formation of a given number of charged pions in $\bar{n}C$ annihilation after full transport and decay.

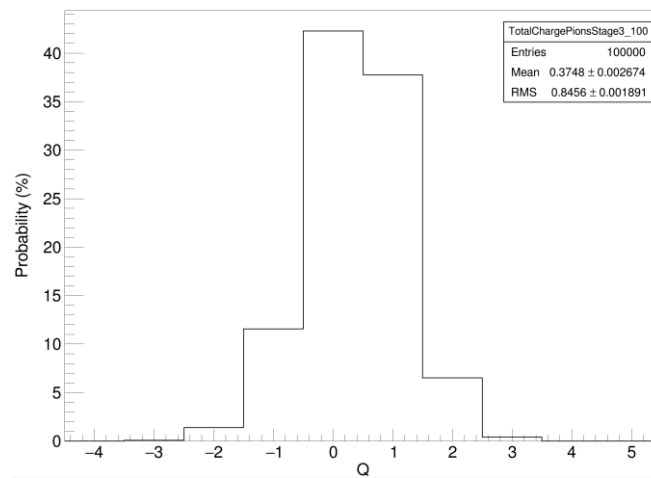


Figure 12. Reproduction of previous Figure 7 with $\bar{n}C$ generator. The distribution of events on particular values of total charge Q transferred to pions emitted from the nucleus; the antineutron and pion potentials are not included.

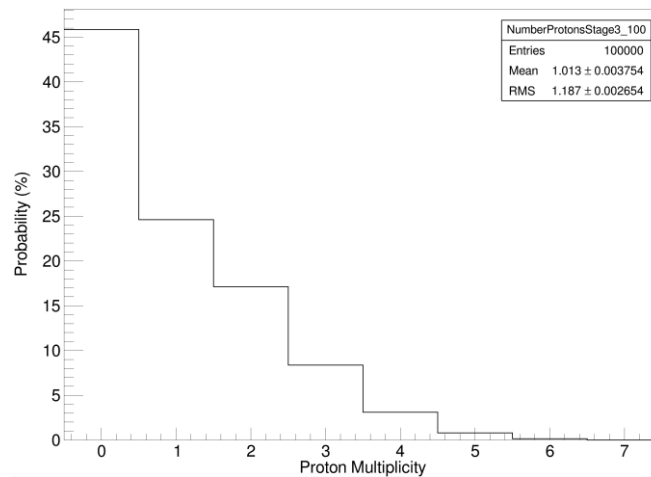


Figure 13. Reproduction of previous Figure 8 with $\bar{n}C$ generator. The distribution of events on the number of exiting protons; the antineutron and pion potentials are not included.

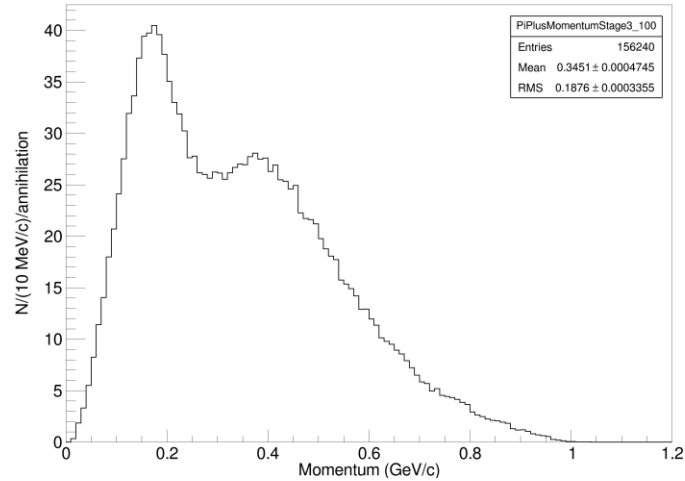


Figure 14. The π^+ momentum distribution is shown, derived from $\bar{n}C$ annihilation; the antineutron and pion potentials are not included.

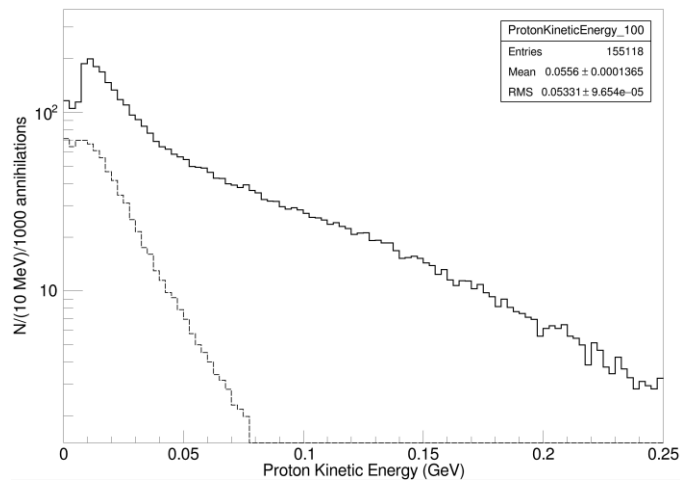


Figure 15. The exiting proton kinetic energy spectrum due to slow antineutron annihilation on carbon nuclei. The solid histogram shows the simulation result. The dotted histogram shows the contribution which evaporative protons impart to the whole distribution. The antineutron and pion potentials are not included.

Another important characteristic for any relativistic many particle system is the invariant mass. One may analyze the invariant mass distribution for annihilation mesons at the annihilation point, and then see how it distorts due to interactions throughout the nucleus. Figure 16 shows how the distribution of invariant mass changes for all outgoing pions and photons resulting $\bar{n}C$ annihilation products (solid), a result of interactions with nuclear media. The dotted line shows the original distribution of invariant mass of the initial $\bar{n}N$ annihilation products.

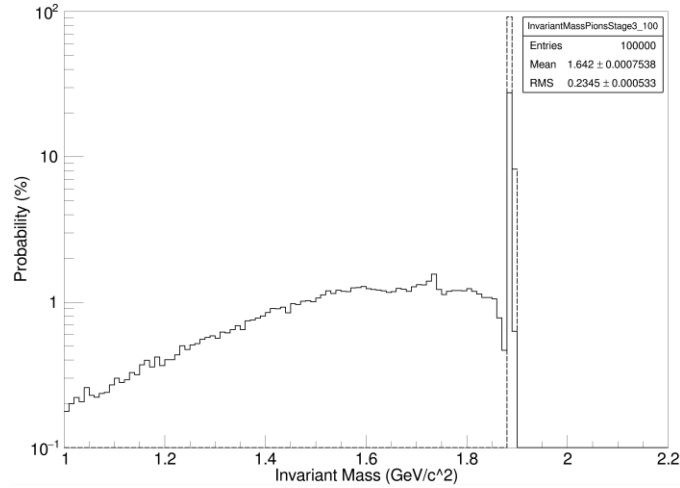


Figure 16. The distribution of invariant mass of annihilation products due to $\bar{\pi}C$ annihilation. The dotted histogram shows the distribution of invariant mass due only to original annihilation mesons. The solid histogram shows the invariant mass of pions and photons emanating from the nucleus after transport.

Figure 16 shows that the intranuclear interactions of annihilation mesons with nucleons has resulted in a significant redistribution of energy between mesons and other nuclear constituents, shifting and smearing the initial distribution of M_{inv} down to values of $\sim 1.2 \frac{GeV}{c^2}$. Note that the higher the initial value of M_{inv} , or the deeper the penetration of the antineutron into the nuclear, the larger the number of mesons which will interact with the nuclear environment, quickly devouring this particular part of the distribution.

Similarly, for Figure 17, we see that the momentum distribution reconstructed from initial annihilation mesons is perturbed and expanded by transport through the nuclear environment. The structure shown in the dotted histogram shows a similar distribution as seen in Figure 3, though implicitly convolved with Figure 1. After transport, this distribution distorts as particles cascade through the nucleus, shifting values up to as far as $\sim 0.8 \frac{GeV}{c}$.

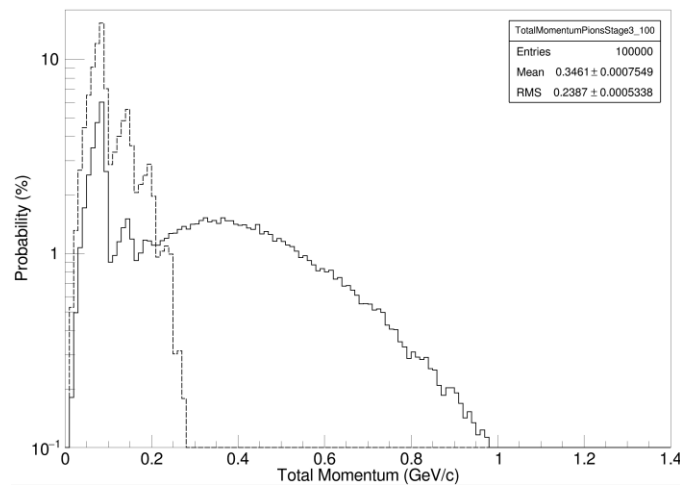


Figure 17. The distribution of total momentum of $\bar{\pi}C$ annihilation products. The dotted histogram shows the distribution of total momentum of all original annihilation mesons. The solid histogram shows the distribution of total momentum of pions and photons emanating from the nucleus after transport.

A less relevant, secondary plot of total momentum versus invariant mass output variables is shown below in Figure 18 for outgoing pions and photons. The projection of the x -axis is precisely Figure 16, while the y -axis is Figure 17. Across Figures 16-18, all bin widths are identical (10 MeV), and all scales are logarithmic, showing probability in percent. Note the bright spot at $\sim 1.9 \frac{\text{GeV}}{c^2}$ in invariant mass and $\sim 0.1 \frac{\text{GeV}}{c}$ in total momentum; this shape curves slightly upward and to the right, and contains the $\sim 35\%$ of all exiting pions and photons which go through the nucleus without interaction.

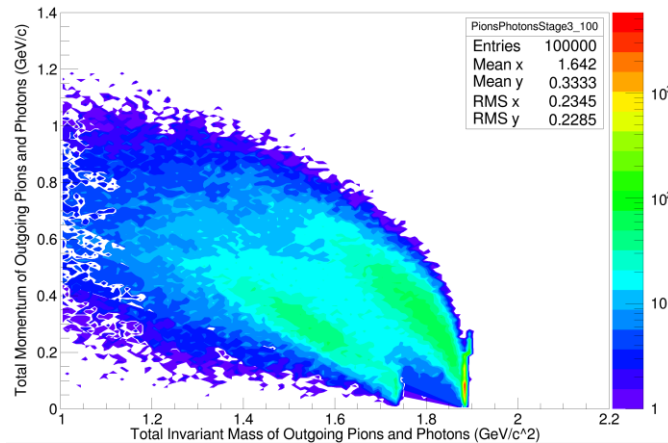


Figure 18: Stage 3 total momentum vs. invariant mass of pions and photons. Note the double lobe structure; this is due to the absorption of a single meson during transport. Also recognize the thin, sickle-like shape in the lower right-hand corner of the figure; these are the remnants of the initial Stage 1 mesons which did not interact with the nucleus.

5. Conclusion

This work has endeavored to explain the detail of the optical-cascade model for describing antineutron annihilation on carbon nuclei. The absorption of a slow antineutron is described in the framework of the optical model. A combination of experimental data with the results of the statistical model employing $SU(3)$ symmetry is used to describe the annihilation process. The propagation of annihilation-produced pions and meson resonances within the nucleus is described by the intranuclear cascade model, which takes into account the nonlinear effect of decreasing nuclear density. The process of de-excitation of residual nuclei is described by a combination of the evaporation model and the Fermi model of explosive disintegration. This combined approach shows good agreement with experimental data in the modeling of antiproton annihilation at rest on carbon nuclei, and provides a reliable predictor of the characteristics of slow antineutron annihilation on carbon. This model can thus be used as an event generator in the design of detector systems for planned experimental searches for neutron-antineutron transformation at the European Spallation Source, employing a free beam of cold (10 meV) neutrons.

This approach is universal, and can be used for simulation an antineutron annihilation on many different nuclei. However, to search for the transformation occurring *within* nuclei (for example, within ${}^{40}_{18}\text{Ar}$, with no external source of antineutrons), a valid model can only be created when a proper definition of radial annihilation probability density is incorporated, allowing for the derivation of intranuclear

transformation constraints. The model proposed in this work can be thought of as a first step in the preliminary modeling of this full process.

Expressing an aside into future developments, it is planned that more precise modeling will be rendered for the intranuclear $n \rightarrow \bar{n}$ transformation thought possibly to take place with ${}^{40}_{18}\text{Ar}$. Proper simulation of such a signal will be important to assess the feasibility of significantly improved transformation searches in the DUNE experiment. The basic physics, model, file types, and analysis techniques presented in this article will continue to be employed, though special care must be taken in the integration of a proper intranuclear transformation and annihilation radial probability distribution into the simulation. One other $n \rightarrow \bar{n}$ generator, already developed internally to the DUNE collaboration, is currently being studied by multiple colleagues in both the DUNE and ESS collaborations; complex techniques have been developed using neural networks to study the separability of supposed signal from atmospheric neutrino background with promising results [40]. However, when considering the subtleties of the simulation assumptions and techniques, some room for improvements within the generator are thought to be possible. Thus, the independent generator development described in this work, along with its future ${}^{40}_{18}\text{Ar}$ cousin, will hopefully lead to a fruitful collaboration and collective meta-analysis between generators and groups, which could reputedly assess the probability of separating signal from background sources in such a large, underground experiment.

In conclusion, the authors would like to thank Jean-Marc Richard and Eduard Paryev for useful discussions of these nuclear processes, and to Yuri Kamyshev for his permanent interest in this work. We wish to thank our colleagues in the NNbar ESS collaboration for the encouragement of this work. The work of JB was partially supported through DOE Grant DE-SC0014558. EG is grateful to the INR, Moscow for supporting her travel.

References

1. V. A. Kuzmin, *Pisma Zh.Eksp.Teor.Fiz.* **12**, 335 (1970) (in Russian).
2. A. D. Sakharov, *ZhEFT Pis'ma* **5**, 32 (1967).
3. M. Baldo-Ceolin, *Zeitschrift für Physik C Particles and Fields* **63**, 409 (1994).
4. D. G. Phillips, *Physics Reports* **612**, 1 (2016).
5. J. Chung, *Physical Review D* **66**, 032004 (2002).
6. C. Adams, arXiv:1307.7335v3 [hep-ex] (2014).
7. K. G. Chetyrkin, M. V. Kazarnovsky, V. A. Kuzmin, and M. E. Shaposhnikov, *Physics Letters B* **99**, 358 (1981).
8. A. S. Iljinov, V. I. Nazaruk, and S. E. Chigrinov, *Nuclear Physics A* **382**, 378 (1982).
9. E. S. Golubeva, A. S. Iljinov, and L. A. Kondratyuk in *Antineutron annihilation event generator for n-nbar search experiment* (Office of Scientific and Technical Information, Oak Ridge, TN, 1996), pp. 295–305.
10. E. S. Golubeva, A. S. Iljinov, and L. A. Kondratyuk, *Physics of Atomic Nuclei* **60**, 2006 (1997).
E. S. Golubeva and L. A. Kondratyuk, *Nuclear Physics B - Proceedings Supplements* **56**, 103 (1997).
11. Y. A. Kamyshev, in *Future prospects for neutron-Antineutron transition searches* (Physics of Atomic Nuclei, Moscow, 1996), pp. 1554–1557.
12. J. Carbonell and K. V. Protasov, *Journal of Physics G: Nuclear and Particle Physics* **18**, 1863 (1992).
13. S. Tessaro, PhD thesis, The University of Trieste, 1995.
14. V. S. Barashenkov, A. S. Iljinov, N. M. Sobolevskii, and V. D. Toneev, *Soviet Physics Uspekhi* **16**, 31 (1973) (in Russian).
15. C. B. Dover, A. Gal, and J. M. Richard, *Physical Review C* **31**, 1423 (1985).
16. W. M. Alberico, in *nnbar Suppression in intranuclear transitions* (Office of Scientific and Technical Information, Oak Ridge, TN, 1996), pp. 221–234.
17. B. O. Kerbikov, arXiv:1704.07117v3 [hep-ph] (2017).
18. C. B. Dover, A. Gal, and J. M. Richard, in *Neutron-Antineutron oscillations at the surface of nuclei* (Office of Scientific and Technical Information, Oak Ridge, TN, 1996), pp. 241–243.
19. Kh. M. Beshtoev, Joint Institute for Nuclear Research Preprints and Communications (in Russian), JINR **P2-5480**, **P2-6337**, Dubna (1972).
20. I. A. Pshenichnov, PhD thesis (in Russian), The Institute for Nuclear Research, Moscow, 1997.
21. E. S. Golubeva, A. S. Iljinov, B. V. Krippa, and I. A. Pshenichno, *Nuclear Physics A* **537**, 393 (1992).
22. E. Klempt, C. Batty, and J. M. Richard, *Physics Reports* **413**, 197 (2005).
23. E. D. Minor, T. A. Armstrong, R. Bishop, V. Harris, R. A. Lewis, and G. A. Smith, *Zeitschrift für Physik A Atomic Nuclei* **336**, 461 (1990).
24. G. Levman, R. Singer, and T. Fields, *Physical Review D* **21**, 1 (1980).
25. R. Hamatsu, *Nuclear Physics B* **123**, 189 (1977).
26. J. Roy, in *Inclusive Properties of anti-p d at Rest Annihilation Products* (Syracuse, New York, n.d.), pp. 1–12.
27. V. E. Bunakov, *Physics of Elementary Particles and Atomic Nuclei* **11** (English translation), 1285 (1980).
28. V. S. Barashenkov, A. S. Iljinov, and V. D. Toneev, *Physics of Atomic Nuclei* **13** (in Russian), 743 (1971).
29. V. Flaminio, I. F. Graf, J. D. Hansen, W. G. Moorhead, and D. R. O. Morrison, CERN-HERA-79-01 286 (1979).
30. A. S. Botvina, A. S. Iljinov, I. N. Mishustin, J. P. Borndorf, R. Donangelo, and K. Sneppen, *Nuclear Physics A* **447**, 663 (1987).
31. L. G. Moretto, in *Study of a fission-like environment in reactions with very heavy ions* (International Atomic Energy Agency, Vienna, 1974), pp. 351–364.
32. A. S. Botvina, E. S. Golubeva, A. S. Iljinov, and I. A. Pshenichnov, *Physics of Atomic Nuclei* (English translation) **55**, (1992).
33. L. E. Agnew, *Physical Review* **118**, 1371 (1960).
34. J. Riedlberger, *Physical Review C* **40**, 2717 (1989).
35. M. Wade and V. G. Lind, *Physical Review D* **14**, 1182 (1976).
36. G. T. Condo, T. Handler, and H. O. Cohn, *Physical Review C* **29**, 1531 (1984).
37. P. L. Mcgaughey, K. D. Bol, M. R. Clover, R. M. Devries, N. J. Digiacomio, J. S. Kapustinsky, W. E. Sondheim, G. R. Smith, J. W. Sunier, Y. Yariv, M. Buenerd, J. Chauvin, D. Lebrun, P. Martin, and J. C. Dousse, *Physical Review Letters* **56**, 2156 (1986).
38. P. Hofmann, F. Hartmann, H. Daniel, T. V. Egidy, W. Kanert, W. Markiel, H. Plendl, H. Machner, G. Riepe, D. Protić, K. Ziock, R. Marshall, and J. Reidy, *Nuclear Physics A* **512**, 669 (1990).
39. R. Brun, F. Rademakers, *ROOT - An Object Oriented Data Analysis Framework*, Proceedings AIHENP'96 Workshop, Lausanne, Sep. 1996, *Nucl. Inst. & Meth. in Phys. Res. A* **389** (1997) 81-86.
40. J. E. T. Hewes, *Searches for Bound Neutron-Antineutron Oscillation in Liquid Argon Time Projection Chambers*, thesis, Faculty of Science and Engineering, 2017.